
# The heart of Sakurai's object revealed by ALMA

A&A 677, L8 (2023)
https://doi.org/10.1051/0004-6361/202347293


Astronomy & Astrophysics

LETTER TO THE EDITOR

# The heart of Sakurai's object revealed by ALMA

Daniel Tafoya[1], Peter A. M. van Hoof[2], Jesús A. Toalá[3], Griet Van de Steene[2], Suzanna Randall[6], Ramlal Unnikrishnan[1], Stefan Kimeswenger[4,5], Marcin Hajduk[7], Daniela Barría[8], and Albert Zijlstra[9]

[1] Department of Space, Earth and Environment, Chalmers University of Technology, Onsala Space Observatory, 439 92 Onsala, Sweden
e-mail: daniel.tafoya@chalmers.se
[2] Royal Observatory of Belgium, Ringlaan 3, 1180 Brussels, Belgium
[3] Instituto de Radioastronomía y Astrofísica, UNAM, Ant. carretera a Pátzcuaro 8701, Ex-Hda. San José de la Huerta, Morelia 58089, Mich., Mexico
[4] Universität Innsbruck, Institut für Astro- und Teilchenphysik, Technikerstr. 25, 6020 Innsbruck, Austria
[5] Universidad Católica del Norte, Instituto de Astronomía, Av. Angamos 0610, Antofagasta, Chile
[6] European Southern Observatory, Karl Schwarzschild str. 2, 85748 Garching, Germany
[7] Space Radio-Diagnostics Research Centre, University of Warmia and Mazury, Prawocheńskiego 9, 10-720 Olsztyn, Poland
[8] Facultad de Ingeniería y Arquitectura, Universidad Central de Chile, Av. Francisco de Aguirre 0405, La Serena, Coquimbo, Chile
[9] Jodrell Bank Centre for Astrophysics, Alan Turing Building, University of Manchester, Manchester M13 9PL, UK

Received 26 June 2023 / Accepted 16 August 2023

**ABSTRACT**

We present high-angular-resolution observations of Sakurai's object using the Atacama Large Millimeter Array, shedding new light on its morpho-kinematical structure. The millimetre continuum emission observed at an angular resolution of 20 milliarcsec (corresponding to 70 AU) reveals a bright compact central component whose spectral index indicates that it is composed of amorphous carbon dust. Based on these findings, we conclude that this emission traces the previously suggested dust disc observed in mid-infrared observations, and therefore our observations provide the first direct imaging of this disc. The $H^{12}CN(J = 4 \rightarrow 3)$ line emission observed at an angular resolution of 300 milliarcsec (corresponding to 1000 AU) displays a bipolar structure with a north–south velocity gradient. From the position–velocity diagram of this emission, we identify the presence of an expanding disc and a bipolar molecular outflow. The inclination of the disc is determined to be $i = 72°$. The derived values for the de-projected expansion velocity and the radius of the disc are $v_{exp} = 53\,km\,s^{-1}$ and $R = 277$ AU, respectively. On the other hand, the de-projected expansion velocity of the bipolar outflow detected in the $H^{12}CN(J = 4 \rightarrow 3)$ emission is of approximately $1000\,km\,s^{-1}$. We propose that the molecular outflow has an hourglass morphology with an opening angle of around 60°. Our observations unambiguously show that an equatorial disc and bipolar outflows formed in Sakurai's object during the 30 years following the occurrence of the born-again event, providing important constraints for future modelling efforts of this phenomenon.

**Key words.** stars: low-mass – binaries: general – stars: winds, outflows – planetary nebulae: general – planetary nebulae: individual: Sakurai's object

## 1. Introduction

Stars with masses of up to $8\,M_{\odot}$ shed most of their hydrogen envelope during the asymptotic giant branch (AGB) phase. As hydrogen- and helium-burning cease in the layers around the core, these stars transition to the early white dwarf sequence where they spend the remainder of their lives as white dwarfs (WDs). Theory predicts that up to one-quarter of these stars experience a 'final helium shell flash' during this stage, where the residual helium spontaneously ignites under degenerate conditions (Iben et al. 1983; Blöcker 2001; Herwig 2005), which triggers a so-called 'born-again event'. During the born-again event, the remaining hydrogen envelope mixes into the stellar core and is burned, leading to a new H-poor and $^{13}$C-rich shell ejection. After this, the star undergoes a double loop in the Hertzsprung-Russell diagram (Lawlor & MacDonald 2003; Hajduk et al. 2005) before helium burning stops, and the star re-enters the WD sequence as an H-poor star. The born-again event is thought to be a likely path for the formation of hydrogen-deficient stars such as non-DA white dwarfs, PG 1159, and [WC] stars, as well as some R CrB stars (Werner & Herwig 2006). Because born-again objects evolve on very short timescales, it is extremely rare to observe the process in action. Indeed, this has been achieved for only two cases: V605 Aql, which experienced a final helium shell flash at the beginning of the 20th century, and V4334 Sgr (also known as Sakurai's object), which was caught undergoing the born-again behaviour in the mid 1990s (Duerbeck et al. 1996). Consequently, the born-again event is still very poorly understood, despite its importance in stellar evolution and evolved stellar populations.

Sakurai's object, whose assumed distance from the Sun is 3.5 kpc (Hinkle et al. 2020), is the only star to have been monitored with modern facilities throughout most of the born-again process. At the time of discovery, Sakurai's object had evolved from the early WD sequence to a born-again red giant just a few years earlier. Soon after that, it became completely enshrouded

by a thick layer of dust (Kimeswenger et al. 1997). Early optical observations provided the first indications that the morphology of the ejecta was bipolar with a thick obscured disc or torus (Tyne et al. 2000; Kerber et al. 2002; Evans et al. 2006; van Hoof et al. 2007). From MiD-Infrared/VLT Interferometer (MIDI/VLTI) observations it was possible to derive a model of the morphology of the ejecta and determine that it contains a dusty disc seen almost edge-on, efficiently screening the central source (Chesneau et al. 2009). In addition, Gemini Near InfraRed Imager/ALTtitude conjugate Adaptive optics for the InfraRed unit (NIRI/ALTAIR) and Near-Infrared Integral Field Spectrometer (NIFS) images of Sakurai's object show a pair of lobes expanding with a velocity of ∼300 km s$^{-1}$, with the northeast and southwest lobes moving away from and toward us, respectively (Hinkle & Joyce 2014; Hinkle et al. 2020). While all these observations point towards some form of bipolar structure, they only give a partial and limited view of the situation. As it is expected that a considerable fraction of the ejected material has cooled down and condensed into molecular gas and dust, observations at longer wavelengths are essential to getting the full picture. In this letter, we present high-angular-resolution Atacama Large Millimeter Array (ALMA) observations, which we use to uncover the morphology of the cool ejecta in the youngest born-again star.

## 2. Observations

We conducted observations of the continuum and molecular line emissions of Sakurai's object using ALMA. The project IDs associated with the observations used in this work are 2017.1.00017.S, 2018.1.00088.S (PI: P. van Hoof), and 2018.1.00341.S (PI: D. Tafoya). All observations were performed using the ALMA 12 m array, which included 43-47 antennas. The relevant parameters of the observations are summarised in Table A.1. The data were calibrated and imaged using the ALMA pipeline, which is included in the Common Astronomy Software Application (CASA; McMullin et al. 2007).

For the continuum emission, we included data from all the observations. However, for the molecular line emission, we only used the data from the observations of project 2018.1.00341.S. The continuum emission was obtained separately for each spectral window using line-free channels. The high-angular-resolution continuum image shown in Fig. 1 was made from only the observations carried out on 22 June, 2019. The continuum emission from four spectral windows centred at 224.0 GHz, 226.0 GHz, 240.0 GHz, and 242.0 GHz was combined, resulting in a total bandwidth of 6.73 GHz. The multi-scale algorithm was used in the cleaning process with the CASA task 'tclean'. The robust parameter of the Briggs weighting scheme and the pixel size of the image were set to 0.5 and 0.004 arcsecs, respectively. The resulting root mean square (rms) of the continuum image is approximately 44 μJy beam$^{-1}$, with a beam size of 0.021 × 0.019 arcsec (P.A.[1] −84.1°).

The spectral data include emission of the H$^{12}$CN($J$ = 4 → 3), H$^{13}$CN($J$ = 4 → 3), and CO($J$ = 3 → 2) lines. The spectral setup of these observations consists of four spectral windows, each of 1.875 GHz in width, centred at frequencies 343.009 GHz, 344.967 GHz, 355.009 GHz, and 356.897 GHz. Each spectral window has 1917 channels with a width of 976.562 kHz. The channel maps were created manually using a robust parameter of 0.0 and a pixel size of 0.06 arcsecs.

[1] The position angle (P.A.), measured north through east, relative to the north celestial pole.

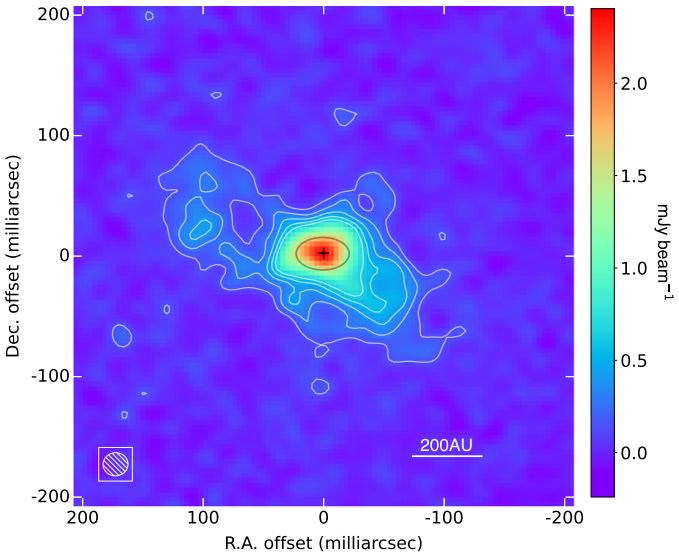


**Fig. 1.** ALMA continuum emission of Sakurai's object at 233 GHz. The emitting regions consist of a bright compact central component and faint extended structures elongated in the northeast-southwest directions. A Gaussian fit to the central component is shown as a grey ellipse. The black cross indicates the continuum peak position at (J2000) RA = 17$^h$52$^m$32$^s$.6990 ± 0$^s$.0002, Dec = −17°41′7.″915 ± 0.″003. The rms noise level of the image is 44 μJy beam$^{-1}$. The horizontal bar indicating the linear scale of the image assumes a distance of 3.5 kpc to the source. The synthesised beam of the ALMA observations is shown in the bottom-left corner and its parameters are: $\theta_{\rm beam}$ = 21 × 19 milliarcsec, P.A. = −84.1°.

The typical rms noise in the individual 0.8 km s$^{-1}$ wide channels is 3 mJy beam$^{-1}$, with a beam size of approximately 0.33 × 0.30 arcsec (P.A. ∼ 73°).

## 3. Results and discussion

### 3.1. Continuum emission: The dust disc of Sakurai's object

The circumstellar dust of Sakurai's object has been extensively studied at infrared (IR) wavelengths (e.g., Geballe et al. 2002; Tyne et al. 2002; Käufl et al. 2003; Chesneau et al. 2009; Hinkle & Joyce 2014; Hinkle et al. 2020; Evans et al. 2020, 2022, and references therein). In contrast, observations of the dust at submillimetre (mm) or longer wavelengths remain limited, with only a few instances reported (e.g., Evans et al. 2004). From an analysis of the evolution of the circumstellar dust in Sakurai's object over an ∼20 year period, Evans et al. (2020) find that, overall, the mid-IR dust emission can be adequately modelled as originating from a blackbody that has cooled from $T_{\rm dust}$ = 1200 K in 1998 to $T_{\rm dust}$ = 180 K in 2016. Additionally, the dust mass has increased from $M_{\rm dust}$ ∼ $10^{-9}$ $M_\odot$ to $M_{\rm dust}$ ∼ $10^{-5}$ $M_\odot$ in the same period. While the mid-IR emission indicates a decline in dust temperature, the increase in continuum emission in the near-IR suggests the formation of new hot dust (Hinkle et al. 2020; Evans et al. 2020, 2022). Therefore, a multi-temperature model to fit both cooling, expanding dust and a hotter near-IR excess is required, and observations at mm and submillimetre (submm) wavelengths are invaluable in order to constrain physical parameters.

Figure 1 shows an image of the 1.3 mm continuum emission of Sakurai's object with an unprecedented angular-resolution of 20 milliarcsec (70 AU). The image reveals an emitting region consisting of a bright compact central component and faint

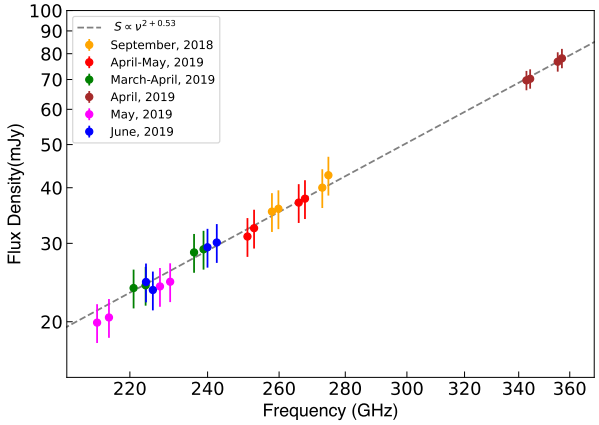


**Fig. 2.** Spectral energy distribution of the ALMA continuum emission of Sakurai's object. The dashed line indicates a fit using a power law function, as described in the main text. The error bars indicate the nominal uncertainty in the absolute calibration of the ALMA observations of 5%.

extended structures elongated along the northeast–southwest direction. The total flux at 233 GHz is 25 mJy and the peak of the emission is located at (J2000) RA = $17^h52^m32\overset{s}{.}6990 \pm 0\overset{s}{.}0002$, Dec = $-17°41'7\overset{''}{.}915 \pm 0\overset{''}{.}003$. A Gaussian fit to the bright compact central component, shown as a grey ellipse in Fig. 1, gives a deconvolved size of $44 \pm 3 \times 27 \pm 2$ milliarcsec ($154 \pm 10 \times 95 \pm 7$ AU) with a P.A. of $90° \pm 6°$. The peak brightness temperature of this component is $T_B = 217$ K. The faint extended emission lies along P.A. $\approx 60°$ with a total length of approximately 230 milliarcsec (800 AU). Both the major axis of the bright compact central component and the axis of elongation of the faint extended structures are rotated compared to the bipolar outflow seen in near-IR images, P.A. = $21° \pm 5°$ (Hinkle et al. 2020), suggesting that the ALMA continuum is not tracing this bipolar outflow. Moreover, the bright compact central component is oriented nearly perpendicularly to the bipolar outflow. Furthermore, its brightness temperature is in excellent agreement with the temperature ($T \approx 200$ K) of the cold dust disc hinted at by mid-IR observations (Chesneau et al. 2009; Hinkle et al. 2020; Evans et al. 2020). This strongly suggests that the mm continuum emission of the bright compact central component is produced by such a cold dust disc[2], implying that our ALMA image is the first direct image of the disc.

Early analysis of IR observations indicated that the circumstellar dust of Sakurai's object primarily consists of graphitic carbon (Eyres et al. 1998; Tyne et al. 2002). Subsequent studies using *Spitzer* Space Telescope and *James Clerk Maxwell* Telescope (JCMT) data suggested that the graphitic carbon fraction decreased, while the amorphous carbon fraction increased (Evans et al. 2004, 2006). Chesneau et al. (2009) noted the absence of spectral features in the MIDI IR spectrum, which these authors interpreted as indicative of the dominance of amorphous carbon grains in the dust composition. Furthermore, Evans et al. (2020) reported evidence for weak 6–7 μm absorption, which these latter authors attribute to hydrogenated amorphous carbon formed in material ejected by Sakurai's object at early stages after the born-again event.

While all of this evidence appears to suggest that the dust is predominantly composed of amorphous carbon, there remains a need for additional constraints on the properties of the dust grains. Some of these constraints can be obtained from the analysis of data taken within the far-IR to mm spectral range. In particular, at mm and submm wavelengths, valuable insights into the characteristics of the emitting dust can be gained by assuming optically thin emission and fitting the observed flux densities to a power law of the form $S_\nu \propto \nu^{2+\beta}$, where $\beta$ represents the dust opacity index. For amorphous carbon, $\beta \approx 0.7-1$, whereas for graphitic carbon, $\beta \approx 2$ (e.g., Mennella et al. 1995, 1998). From our ALMA observations, we obtained the continuum flux densities of Sakurai's object for the frequency range 212–357 GHz. The fluxes were measured by integrating a region containing emission exceeding three times the rms noise level of the image, and they are listed in Table A.2 and shown in Fig. 2. A power-law fit to the data gives an opacity index of $\beta = 0.53 \pm 0.03$. It is noteworthy that, up to this point, this value represents the most precisely determined dust opacity index for this source within the mm and submm wavelengths range. This value is close to that expected for the sample BE of amorphous carbon analogues studied by Mennella et al. (1998), albeit slightly smaller. The reason for this could be, as Evans et al. (2004) points out, that the emission is produced by large grains and/or there has been an increase in the population of hotter grains (which have flatter emissivities).

Assuming isothermal dust with a temperature $T_{\rm dust} = 217$ K (i.e., assuming that the peak continuum emission is optically thick) and that most of the dust emission is optically thin, the mass of the dust can be obtained using the following expression:

$$M_{\rm dust} = \frac{S_\nu D^2}{\kappa_\nu B_\nu(T_{\rm dust})},$$

where $S_\nu$ is the flux density of the continuum emission, $D$ is the distance to the source, $\kappa_\nu = \kappa_0(\nu/\nu_0)^\beta$ is the dust absorption coefficient, and $B_\nu(T)$ is the Planck function. Dust absorption coefficient of amorphous carbon in the literature range from $\kappa_{300\,\rm GHz} \sim 0.9\,{\rm cm^2\,g^{-1}}$ up to $\kappa_{300\,\rm GHz} \sim 90\,{\rm cm^2\,g^{-1}}$ (Draine & Lee 1984; Ossenkopf & Henning 1994; Mennella et al. 1998; Suh 2000). Using the dust opacity index obtained from our ALMA observations ($\beta = 0.53 \pm 0.03$, see Fig. 2), the calculated mass of amorphous carbon dust in Sakurai's object is therefore $6 \times 10^{-3}\,M_\odot$ and $6 \times 10^{-5}\,M_\odot$ for $\kappa_{300\,\rm GHz} \sim 0.9\,{\rm cm^2\,g^{-1}}$ and $\kappa_{300\,\rm GHz} \sim 90\,{\rm cm^2\,g^{-1}}$, respectively. Estimations of the dust mass based on mid-IR observations range from 1.8 to $6 \times 10^{-5}\,M_\odot$ (Chesneau et al. 2009; Hinkle et al. 2020; Evans et al. 2020). Therefore, in order to obtain a dust mass consistent with these previous estimations, it is necessary to consider amorphous carbon dust with a relatively large absorption coefficient in the submm wavelength regime.

### 3.2. Line emission: An expanding disc and a fast bipolar outflow in Sakurai's object

Carbon-rich molecules (CN, $C_2$, CO) were detected in the ejecta of Sakurai's object as early as one year after it was discovered to be undergoing the born-again event (Eyres et al. 1998). Subsequently, H-containing species (e.g., HCN and $C_2H_2$) were also found in the ejected material (Evans et al. 2006). All of these molecular species were detected against the dust continuum emission, probing primarily the molecular gas along the line-of-sight direction. More recently, Tafoya et al. (2017) detected emission of $H^{12}CN(J = 4 \rightarrow 3)$, $H^{13}CN(J = 4 \rightarrow 3)$, and $H^{12}CN(J = 2 \rightarrow 1)$ lines for the first time, and van Hoof et al. (2018) presented semi-resolved ALMA images of the line of

[2] The structure referred to as a 'disc' may also exhibit a torus-like morphology, but for consistency with the nomenclature in the literature, we refer only to discs unless indicating otherwise.

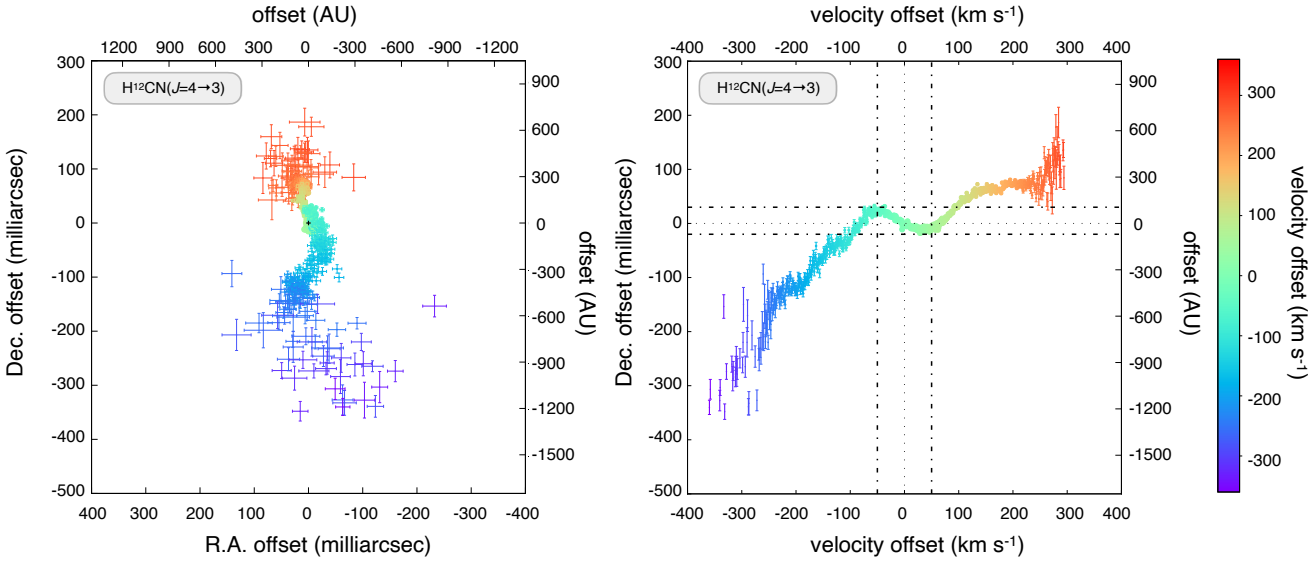


**Fig. 3.** Spatial-kinematical distribution of the $H^{12}CN(J = 4 \rightarrow 3)$ line emission in Sakurai's object. *Left:* spatial distribution of the centroid positions of the $H^{12}CN(J = 4 \rightarrow 3)$ line emission at each individual velocity channel. *Right:* position–velocity diagram of the $H^{12}CN(J = 4 \rightarrow 3)$ line emission centroids along the Declination axis. The vertical and horizontal dashed lines indicate the velocity offset and Declination offset, respectively, over which an inversion of the velocity gradient is observed. The error bars correspond to the uncertainties of the centroid positions. The axis indicating the linear scale assumes a distance of 3.5 kpc to the source.

emission of CN, CO, and $HC_3N$. While these observations suggest that the CO molecules are situated in proximity to the dusty region (Eyres et al. 2004; Worters et al. 2009; van Hoof et al. 2018), the HCN and CN are believed to reside in bipolar lobes (Evans et al. 2006; van Hoof et al. 2018). However, due to the limited angular resolution of previous observations, it has not been possible to discern the specific regions from which the molecular emission originates.

To further investigate the molecular component of the ejecta around Sakurai's object, we conducted ALMA observations targeting the $H^{12}CN(J = 4 \rightarrow 3)$, $H^{13}CN(J = 4 \rightarrow 3)$, and $CO(J = 3 \rightarrow 2)$ line emissions. These observations provided an angular resolution of approximately 300 milliarcsec (~1000 AU) and a spectral resolution of 0.8 km s$^{-1}$. Figure B.1 shows the spectra obtained from the ALMA observations, alongside the spectra acquired using the Atacama Pathfinder Experiment (APEX) in 2013 and 2016 (Tafoya et al. 2017). Due to the lower S/N of the APEX spectra, accurately measuring any changes in the brightness of the $H^{12}CN(J = 4 \rightarrow 3)$ and $H^{13}CN(J = 4 \rightarrow 3)$ lines between the APEX and ALMA observations is challenging. However, the spectrum in the right panel of Fig. B.1 clearly shows that the $CO(J = 3 \rightarrow 2)$ line observed in the ALMA data was either not detected or was significantly weaker in the APEX observations. This could be the result of either the recent formation of significant amounts of CO molecules or changes in the physical conditions of the emitting gas. We note that although CO molecules were found in the newly formed ejecta of Sakurai's object (Eyres et al. 1998; Pavlenko et al. 2004), they were detected through absorption features in the near-IR spectra, which is sensitive to even small amounts of CO. Consequently, the cause of the observed enhancement in the $CO(J = 3 \rightarrow 2)$ line intensity remains uncertain.

The widths of the molecular lines are notably broad. The velocity offset range covered by the $H^{12}CN(J = 4 \rightarrow 3)$ line extends from −350 km s$^{-1}$ to 300 km s$^{-1}$, with the redshifted portion even exceeding the bandwidth of our spectral window. In contrast, the $H^{13}CN(J = 4 \rightarrow 3)$ and $CO(J = 3 \rightarrow 2)$ lines are blended, preventing us from spatially separating their emissions. Furthermore, the blueshifted part of the $CO(J = 3 \rightarrow 2)$ line also extends beyond the limits of our spectral window. Despite these limitations, the significantly higher spectral resolution of the ALMA observations enables the identification of distinct velocity components for each molecule. Additionally, the achieved high S/N allows precise determination of the centroid of the molecular emission in each velocity channel, surpassing the size of the synthesised beam (Condon 1997). Specifically, the uncertainties of the centroid positions are obtained as $\sigma_{\rm centroid} = (\sigma_\theta^2 + \sigma_{\rm BP}^2)^{1/2}$, where $\sigma_\theta \approx \theta_{\rm beam}/(2$ S/N) and $\sigma_{\rm BP} = \theta_{\rm beam}(\sigma_\phi/360^\circ)$. In these expressions, $\theta_{\rm beam}$ is the beam size and $\sigma_\phi$ is the phase noise of the bandpass calibrator (e.g., Zhang et al. 2017). For our observations, $\theta_{\rm beam}$ = 300 milliarcsecs and $\sigma_\phi = 0.08^\circ$.

Figure 3 presents the spatial distribution and a position–velocity (PV) diagram of the $H^{12}CN(J = 4 \rightarrow 3)$ line emission. The emission exhibits a clear north–south velocity gradient, with the blueshifted and redshifted components positioned to the south and north of the peak of the continuum emission, respectively. The spatial distributions and PV diagrams of the $H^{13}CN(J = 4 \rightarrow 3)$ and $CO(J = 3 \rightarrow 2)$ lines show similar characteristics to those of the $H^{12}CN(J = 4 \rightarrow 3)$ line, but their emitting region appears more compact. This aligns perfectly with the direction and velocity gradient of the near-IR outflow (Hinkle et al. 2020), confirming that the $H^{12}CN(J = 4 \rightarrow 3)$ line emission indeed traces the bipolar outflow of Sakurai's object.

Upon closer examination of the PV diagram, it becomes evident that there is a distinctive change in the velocity gradient. In the central region, where velocity offsets range from −50 to 50 km s$^{-1}$ (see right panel of Fig. 3), the slope is inverted. The horizontal dashed lines in the PV diagram indicate that this emission extends over approximately 50 milliarcsec (~175 AU), which is comparable to the size of the dust disc observed in the ALMA continuum image. This particular pattern of an inverted velocity gradient is commonly observed in systems that exhibit both a bipolar outflow and an expanding equatorial disc (e.g.,

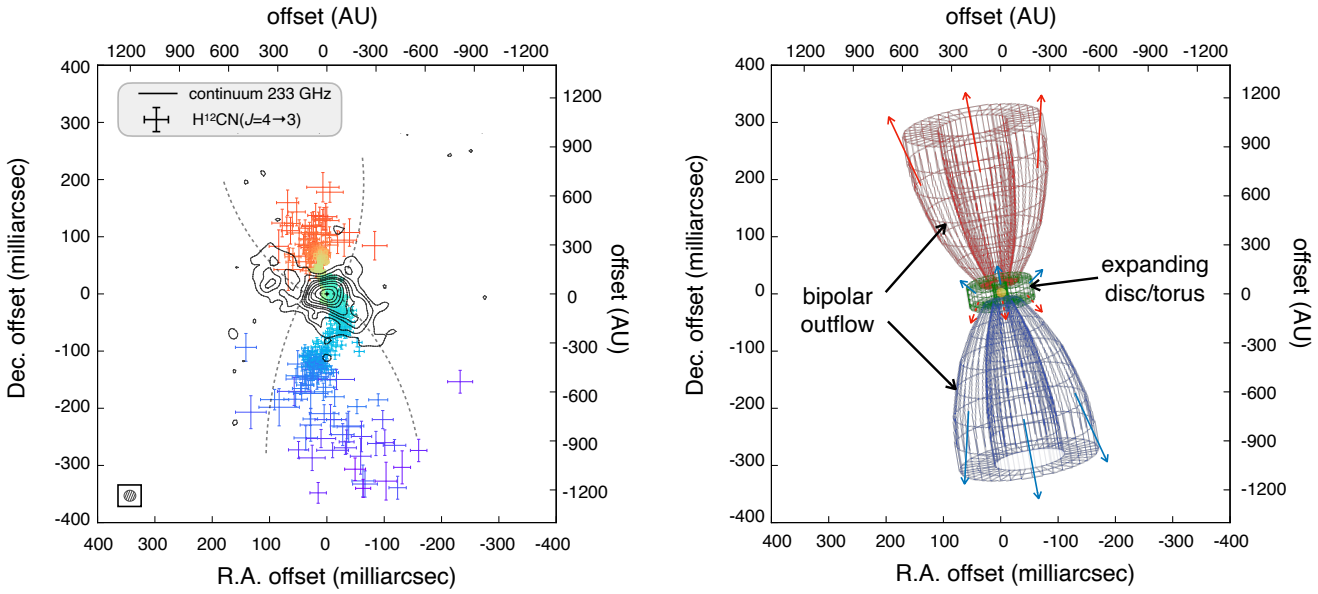


**Fig. 4.** Bipolar outflow and expanding disc around Sakurai's object. *Left:* $H^{12}CN(J = 4 \rightarrow 3)$ line emission and 233 GHz continuum emission. The dashed lines delineate the hourglass morphology suggested by the continuum emission. *Right:* hourglass model for the spatial-kinematical distribution of the bipolar outflow in Sakurai's object. The right and top axes indicate the linear scale assuming a distance of 3.5 kpc to the source.

Alcolea et al. 2007). Thus, it is likely that the inverted velocity gradient is produced by the expansion of the equatorial disc seen in the mm continuum image (see Fig. 1).

For an expanding circular thin disc of radius $R$, whose polar axis has an inclination $i$ with respect to the line of sight, that is $i = 0°$ and $i = 90°$ correspond to the disc seen face-on and edge-on, respectively, the projected minor axis in angular units, $\theta_{\rm disc}$, and its line-of-sight velocity, $v_{\rm los}$, are given by: $\theta_{\rm disc} = 2R\cos i/D$ and $v_{\rm los} = v_{\rm exp}\sin i$, respectively, where $D$ is the distance to the source and $v_{\rm exp}$ is the expansion velocity of the disc. Assuming a constant expansion velocity, the radius of the disc can be calculated as $R = v_{\rm exp}\,\tau$, where $\tau$ is the time since the ejection of the molecular gas. Therefore, the inclination of the disc can be obtained from the following expression:

$$\tan i = 3.0 \left[\frac{v_{\rm los}}{50\,{\rm km\,s^{-1}}}\right]\left[\frac{\tau}{25\,{\rm years}}\right]\left[\frac{\theta_{\rm disc}}{50\,{\rm milliarcsec}}\right]^{-1}\left[\frac{D}{3.5\,{\rm kpc}}\right]^{-1}.$$

From our observations, we find that $v_{\rm los} = 50\,{\rm km\,s^{-1}}$ and $\theta_d = 50$ milliarcsec, and considering that the ejection of the material occurred around 25 years ago, the resulting inclination of the disc is $i = 72°$. This result confirms that the equatorial disc is seen almost edge-on, completely obscuring the central star (Chesneau et al. 2009; Hinkle et al. 2020). The de-projected expansion velocity and the radius of the disc are $v_{\rm exp} = 53\,{\rm km\,s^{-1}}$ and $R = 277$ AU, respectively.

We note that the inclination of the disc derived from our ALMA observations is opposite to that deduced from the VLTI observations (Chesneau et al. 2009). While the VLTI observations suggest that the northern side of the disc is tipped towards us, which would mean that the northern edge of the expanding disc is redshifted, the ALMA observations yield the opposite for the inner 50 milliarcsec: blueshifted emission towards the north and redshifted emission towards the south (cf. right panel of Fig. 3). Furthermore, the inclination obtained from the VLTI observations implies that the northern part of the outflow should be redshifted, which is opposite to the velocity gradient seen from the near-IR and ALMA observations. We therefore conclude that the southern side of the disc is the side tipped towards us.

The derived inclination provides an estimate of the de-projected expansion velocity of the bipolar outflow detected through the $H^{12}CN(J = 4 \rightarrow 3)$ emission, which is approximately 1000 km s$^{-1}$, assuming a fairly collimated structure. Such high expansion velocities for the bipolar outflow of Sakurai's object are not unexpected. For instance, when correcting for the inclination, the expansion velocity of the He I 10830 Å emission line observed with the Gemini NIFS shows a similar value. Also, Kerber et al. (2002) concluded that the bipolar outflow traced by the [N II] $\lambda$6583 line emission exhibited an expansion velocity of about 800 km s$^{-1}$. It is worth noting that such a high expansion velocity implies that the observed lobes should be more than four times larger than observed, assuming that the molecular bipolar outflow formed at the same time as the rest of the material was ejected. This could indicate that the $H^{12}CN(J = 4 \rightarrow 3)$ emission does not fully trace the entirety of the molecular outflow but only the regions where the excitation conditions required to observe HCN molecules are optimal. On the other hand, we cannot dismiss the possibility that the outflow traced by the $H^{12}CN(J = 4 \rightarrow 3)$ emission has a relatively wide opening angle. In such a case, the expansion velocity of the molecular material would be lower, which could explain the smaller observed size of the molecular lobes.

The left panel of Fig. 4 shows the continuum emission superimposed on the spatial distribution of the $H^{12}CN(J = 4 \rightarrow 3)$ line emission. Towards the north, the continuum emission shows two protrusions that appear to be tracing the base of an hourglass-shaped outflow (indicated by the dashed lines). On the southern side, the continuum emission exhibits another such protrusion. A sketch of the inferred geometry and orientation of the material around Sakurai's object is shown in the right panel of Fig. 4. As suggested by the protrusions in the continuum emission, the bipolar outflow lobes have an opening angle of around 60° and their walls seem to be denser than the regions close to the polar axis. In addition, as mentioned above, the spatio-kinematical configuration of the molecular emission is the same as that derived

from observations of the He I 10830Å and the [C I] 9850Å lines (Hinkle et al. 2020). It is therefore possible that the expanding atomic gas forms a more collimated outflow that entrains the surrounding molecular material around it, forging the molecular outflow.

## 4. Concluding remarks

It is remarkable that most known objects that are thought to have experienced a born-again event (A30, A78, V605 Aql, Sakurai's object) have a strikingly similar morphology, namely an expanding equatorial disc and a bipolar outflow (Toalá et al. 2015; Hinkle et al. 2020; Tafoya et al. 2022; Rodríguez-González et al. 2022). The formation of this particular morphology has most often been attributed to a stellar/substellar binary companion. For example A30, a common-envelope phase following the born-again event has been proposed to explain the observed physical structure and abundances of the ejecta around the central star (Rodríguez-González et al. 2022). Tafoya et al. (2022) proposed a similar common-envelope scenario to account for the expanding equatorial structure and bipolar outflow seen in their ALMA observations of V605 Aql. In contrast, standard models of the born-again event are based on single-star evolution that would result in a simple, spherical morphology of the ejecta. This has so far been observed in only one case, HuBi 1 (Toalá et al. 2021; Rechy-García et al. 2020). It is difficult to explain the more complex morphology observed for the other observed objects without invoking common envelope evolution, which would necessitate a paradigm shift because close-binary interactions would certainly influence the physics of the born-again process.

Our ALMA observations reveal, in unprecedented detail, the morpho-kinematical structure of the material surrounding the youngest born-again star, allowing us to study the initial stages of the ejection process. Our results set stringent observational constraints for future models, which will need to be consistent not only with the observed chemistry, but also the physical structure and intriguing morphology observed in the different stages of the born-again process.

*Acknowledgements.* This paper makes use of the following ALMA data: ADS/JAO.ALMA # 2017.1. 00017.S, 2018.1.00088.S and 2018.1.00341.S. ALMA is a partnership of ESO (representing its member states), NSF (USA) and NINS (Japan), together with NRC (Canada), MOST and ASIAA (Taiwan), and KASI (Republic of Korea), in cooperation with the Republic of Chile. The Joint ALMA Observatory is operated by ESO, AUI/NRAO and NAOJ. D.T. acknowledges support from Onsala Space Observatory for the provisioning of its facilities support. The Onsala Space Observatory national research infrastructure is funded through Swedish Research Council grant No 2017-00648. M.H. thanks the Ministry of Education and Science of the Republic of Poland for support and granting funds for the Polish contribution to the International LOFAR Telescope (arrangement no. 2021/WK/02) and for maintenance of the LOFAR PL-612 Baldy station (MSHE decision no. 28/530020/SPUB/SP/2022). The authors also thank the anonymous referee for constructive comments and suggestions that helped to improve the manuscript.

## References

Alcolea, J., Neri, R., & Bujarrabal, V. 2007, A&A, 468, L41
Blöcker, T. 2001, Ap&SS, 275, 1
Chesneau, O., Clayton, G. C., Lykou, F., et al. 2009, A&A, 493, L17
Condon, J. J. 1997, PASP, 109, 166
Draine, B. T., & Lee, H. M. 1984, ApJ, 285, 89
Duerbeck, H. W., Pollacco, D., Verbunt, F., et al. 1996, IAU Circ., 6328
Evans, A., Geballe, T. R., Tyne, V. H., et al. 2004, MNRAS, 353, L41
Evans, A., Tyne, V. H., van Loon, J. T., et al. 2006, MNRAS, 373, L75
Evans, A., Gehrz, R. D., Woodward, C. E., et al. 2020, MNRAS, 493, 1277
Evans, A., Banerjee, D. P. K., Geballe, T. R., et al. 2022, MNRAS, 511, 713
Eyres, S. P. S., Evans, A., Geballe, T. R., Salama, A., & Smalley, B. 1998, MNRAS, 298, L37
Eyres, S. P. S., Geballe, T. R., Tyne, V. H., et al. 2004, MNRAS, 350, L9
Geballe, T. R., Evans, A., Smalley, B., Tyne, V. H., & Eyres, S. P. S. 2002, Ap&SS, 279, 39
Hajduk, M., Zijlstra, A. A., Herwig, F., et al. 2005, Science, 308, 231
Herwig, F. 2005, ARA&A, 43, 435
Hinkle, K. H., & Joyce, R. R. 2014, ApJ, 785, 146
Hinkle, K. H., Joyce, R. R., Matheson, T., Lacy, J. H., & Richter, M. J. 2020, ApJ, 904, 34
Iben, I., Jr, Kaler, J. B., Truran, J. W., & Renzini, A. 1983, ApJ, 264, 605
Käufl, H. U., Koller, J., & Kerber, F. 2003, A&A, 406, 981
Kerber, F., Pirzkal, N., De Marco, O., et al. 2002, ApJ, 581, L39
Kimeswenger, S., Gratl, H., Kerber, F., et al. 1997, IAU Circ., 6608, 1
Lawlor, T. M., & MacDonald, J. 2003, ApJ, 583, 913
McMullin, J. P., Waters, B., Schiebel, D., Young, W., & Golap, K. 2007, in Astronomical Data Analysis Software and Systems XVI, eds. R. A. Shaw, F. Hill, & D. J. Bell, ASP Conf. Ser., 376, 127
Mennella, V., Colangeli, L., & Bussoletti, E. 1995, A&A, 295, 165
Mennella, V., Brucato, J. R., Colangeli, L., et al. 1998, ApJ, 496, 1058
Ossenkopf, V., & Henning, T. 1994, A&A, 291, 943
Pavlenko, Y. V., Geballe, T. R., Evans, A., et al. 2004, A&A, 417, L39
Rechy-García, J. S., Guerrero, M. A., Santamaría, E., et al. 2020, ApJ, 903, L4
Rodríguez-González, J. B., Santamaría, E., Toalá, J. A., et al. 2022, MNRAS, 514, 4794
Suh, K.-W. 2000, MNRAS, 315, 740
Tafoya, D., Toalá, J. A., Vlemmings, W. H. T., et al. 2017, A&A, 600, A23
Tafoya, D., Toalá, J. A., Unnikrishnan, R., et al. 2022, ApJ, 925, L4
Toalá, J. A., Guerrero, M. A., Todt, H., et al. 2015, ApJ, 799, 67
Toalá, J. A., Lora, V., Montoro-Molina, B., Guerrero, M. A., & Esquivel, A. 2021, MNRAS, 505, 3883
Tyne, V. H., Eyres, S. P. S., Geballe, T. R., et al. 2000, MNRAS, 315, 595
Tyne, V. H., Evans, A., Geballe, T. R., et al. 2002, MNRAS, 334, 875
van Hoof, P. A. M., Hajduk, M., Zijlstra, A. A., et al. 2007, A&A, 471, L9
van Hoof, P. A. M., Kimeswenger, S., Van de Steene, G., et al. 2018, Galaxies, 6, 79
Werner, K., & Herwig, F. 2006, PASP, 118, 183
Worters, H. L., Rushton, M. T., Eyres, S. P. S., Geballe, T. R., & Evans, A. 2009, MNRAS, 393, 108
Zhang, Q., Claus, B., Watson, L., & Moran, J. 2017, ApJ, 837, 53

## Appendix A: ALMA Observations

**Table A.1.** Parameters of the ALMA observations

| Observation date (YYYY-MM-DD) | Frequency[a] (GHz) | Flux & Bandpass calibrator (name, Jy) | Phase calibrator (name, mJy) | Bandwidth[b] (GHz) | rms[c] ($\mu$Jy beam$^{-1}$) | Beam (mas×mas,degree)[c] |
|---|---|---|---|---|---|---|
| Project code: 2017.1.00017.S | | | | | | |
| 2018-09-28 | 257.049 | J1924-2914, 2.977 | J1743-1658, 142.5±0.8 | 1.86 | 130 | 268×218, 69.7 |
| | 258.911 | 2.963 | 142.2±0.8 | 0.91 | 130 | 264×214, 69.6 |
| | 272.041 | 2.868 | 138.6±0.8 | 0.82 | 160 | 252×204, 68.8 |
| | 273.904 | 2.855 | 139.1±0.7 | 1.64 | 160 | 251×204, 68.6 |
| Project code: 2018.1.00088.S | | | | | | |
| 2019-05-01 | 212.043 | J1924-2914, 2.746 | J1743-1658, 143.4±0.9 | 1.52 | 31 | 515×454, −79.9 |
| | 214.933 | 2.723 | 142.8±1.0 | 1.86 | 30 | 514×452, −81.1 |
| | 227.357 | 2.634 | 139.6±1.0 | 0.89 | 37 | 487×431, −81.4 |
| | 230.038 | 2.616 | 138.6±1.0 | 0.86 | 40 | 482×425, −81.4 |
| 2019-03-31[2019-04-11][d] | 220.945 | J1924-2914[J1517-2422], 2.900[2.453] | J1743-1658, 157.0±0.8[145.0±0.5] | 1.16 | 48 | 792×571, −88.1 |
| | 223.944 | J1924-2914[J1517-2422], 2.875[2.443] | 155.9±0.8[144.3±0.5] | 1.85 | 41 | 780×560, −88.5 |
| | 236.454 | J1924-2914[J1517-2422], 2.776[2.402] | 151.9±0.9[140.0±0.6] | 1.21 | 54 | 745×533, −88.9 |
| | 238.941 | J1924-2914[J1517-2422], 2.757[2.394] | 151.2±0.7[139.5±0.6] | 1.85 | 52 | 735×531, −88.9 |
| 2019-04-30[2019-05-01][d] | 250.982 | J1924-2914, 2.483 | J1743-1658, 130.8±0.9[126.4±0.9] | 1.25 | 57 | 492×403, 89.2 |
| | 252.850 | 2.472 | 130.2±0.9[126.5±1.0] | 1.41 | 57 | 486×400, 88.9 |
| | 265.808 | 2.400 | 126.9±0.7[123.7±1.0] | 1.08 | 70 | 472×412, −66.9 |
| | 267.677 | 2.390 | 126.4±0.7[122.9±0.7] | 1.19 | 71 | 458×381, 89.8 |
| 2019-06-22 | 224.000 | J1924-2914, 2.913 | J1743-1658, 157.0±1.0 | 1.75 | 73 | 25×24, 48.2 |
| | 226.000 | 2.898 | 156.1±0.6 | 1.48 | 73 | 24×23, −82.8 |
| | 240.000 | 2.795 | 152.6±0.8 | 1.75 | 77 | 23×22, −89.4 |
| | 242.000 | 2.782 | 151.8±0.7 | 1.75 | 84 | 23×21, −87.2 |
| Project code: 2018.1.00341.S | | | | | | |
| 2019-04-21 | 343.009 | J1924-2914, 2.051 | J1742-1517, 149.2±0.4 | 1.37 | 240 | 335×303, 77.3 |
| | 344.967 | 2.044 | 148.7±0.4 | 0.79 | 260 | 336×309, 72.0 |
| | 355.009 | 2.008 | 147.8±0.5 | 0.76 | 290 | 326×298, 73.8 |
| | 356.897 | 2.002 | 147.1±0.5 | 1.36 | 280 | 323×293, 76.8 |

[a] Central frequency of the spectral window. [b] Effective bandwidth of the spectral window used to produce the continuum images. [c] rms noise over the effective bandwidth used to produce the continuum images. [d] mas=milliarcsec. [e] Data taken at two different dates were used to produce the continuum images.

**Table A.2.** Frequency and flux density measurements

| Frequency (GHz)[a] | Flux Density (mJy)[b] |
|---|---|
| 212.071 | 19.91 |
| 214.908 | 20.45 |
| 220.918 | 23.81 |
| 223.913 | 24.15 |
| 224.006 | 24.57 |
| 225.733 | 23.57 |
| 227.537 | 24.01 |
| 230.150 | 24.60 |
| 236.392 | 28.63 |
| 238.911 | 29.10 |
| 239.974 | 29.40 |
| 242.482 | 30.13 |
| 250.953 | 31.08 |
| 252.820 | 32.45 |
| 257.927 | 35.36 |
| 259.805 | 35.88 |
| 265.775 | 37.04 |
| 267.645 | 37.80 |
| 272.886 | 40.02 |
| 274.756 | 42.68 |
| 342.960 | 69.70 |
| 344.387 | 70.27 |
| 355.186 | 76.75 |
| 356.856 | 78.11 |

**Notes.** [(a)]Central frequency of the bandwidth used to create the continuum images. [(b)]Flux density obtained by integrating a region containing emission exceeding 3 times the rms noise level of the image. The nominal uncertainty in the absolute calibration of the ALMA observations of 10% is adopted.

## Appendix B: Additional Figure

Fig. B.1 shows Sakurai's object $H^{12}CN(J=4\rightarrow3)$, $H^{13}CN(J=4\rightarrow3)$ and $CO(J=3\rightarrow2)$ line emission observed by ALMA and APEX.

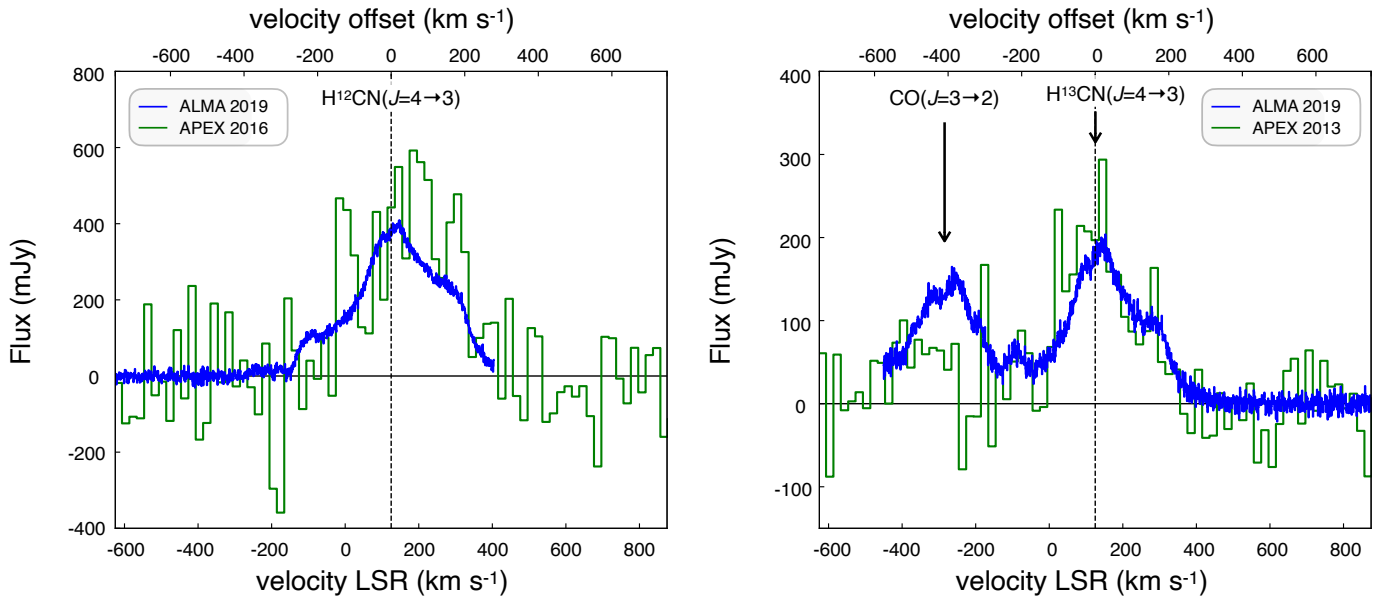


**Fig. B.1.** Sakurai's Object $H^{12}CN(J=4\rightarrow3)$, $H^{13}CN(J=4\rightarrow3)$ and $CO(J=3\rightarrow2)$ line emission. The green line is the spectrum of the emission line detected previously with APEX. The blue line is the spectrum observed with ALMA. The spectral resolutions of the APEX and ALMA observations are 20 km s$^{-1}$ and 0.8 km s$^{-1}$, respectively. The bottom axis indicates the local standard of rest velocity and the top axis indicates the velocity offset from the systemic velocity assumed to be 125 km s$^{-1}$.